

## Naval Research Laboratory Multiscale Targeting Guidance for T-PARC and TCS-08

CAROLYN A. REYNOLDS AND JAMES D. DOYLE

*Marine Meteorology Division, Naval Research Laboratory, Monterey, California*

RICHARD M. HODUR

*Science Applications International Corporation, Monterey, California*

HAO JIN

*Marine Meteorology Division, Naval Research Laboratory, Monterey, California*

(Manuscript received 7 April 2009, in final form 29 September 2009)

### ABSTRACT

As part of The Observing System Research and Predictability Experiment (THORPEX) Pacific Asian Regional Campaign (T-PARC) and the Office of Naval Research's (ONR's) Tropical Cyclone Structure-08 (TCS-08) experiments, a variety of real-time products were produced at the Naval Research Laboratory during the field campaign that took place from August through early October 2008. In support of the targeted observing objective, large-scale targeting guidance was produced twice daily using singular vectors (SVs) from the Navy Operational Global Atmospheric Prediction System (NOGAPS). These SVs were optimized for fixed regions centered over Guam, Taiwan, Japan, and two regions over the North Pacific east of Japan. During high-interest periods, flow-dependent SVs were also produced. In addition, global ensemble forecasts were produced and were useful for examining the potential downstream impacts of extratropical transitions. For mesoscale models, TC forecasts were produced using a new version of the Coupled Ocean–Atmosphere Mesoscale Prediction System (COAMPS) developed specifically for tropical cyclone prediction (COAMPS-TC). In addition to the COAMPS-TC forecasts, mesoscale targeted observing products were produced using the COAMPS forecast and adjoint system twice daily, centered on storms of interest, at a 40-km horizontal resolution. These products were produced with 24-, 36-, and 48-h lead times. The nonhydrostatic adjoint system used during T-PARC/TCS-08 contains an exact adjoint to the explicit microphysics. An adaptive response function region was used to target favorable areas for tropical cyclone formation and development. Results indicate that forecasts of tropical cyclones in the western Pacific are very sensitive to the initial state.

### 1. Introduction

Tropical cyclones (TCs), including hurricanes in the Atlantic and typhoons in the western Pacific, are of great military and civilian interest around the world. To improve the prediction of TC intensity, structure, and track, The Observing System Research and Predictability Experiment (THORPEX; information online at [http://www.wmo.int/pages/prog/arep/wwrp/new/thorpex\\_new.html](http://www.wmo.int/pages/prog/arep/wwrp/new/thorpex_new.html)) Pacific Asian Regional Campaign (T-PARC) and the Office of Naval Research's (ONR's) Tropical Cyclone Structure-08 (TCS-08) field campaign were conducted

from August through early October 2008 (Elsberry and Harr 2008). This international campaign, with nine participating nations, aimed to observe TCs and their environment throughout their life cycles. To accomplish this, five aircraft stationed in Guam, Japan, and Taiwan flew a total of 76 missions, during which almost 1500 vertical soundings of atmospheric data (dropsondes; Hock and Franklin 1999) were taken via instruments dropped from the aircraft. In addition, over 200 soundings were taken from instruments dropped from high-altitude balloons (driftsondes; Cole and Hock 2005) drifting westward from their launch site in Hawaii.<sup>1</sup> There were several

---

*Corresponding author address:* Carolyn Reynolds, Naval Research Laboratory, 7 Grace Hopper Ave., Monterey, CA 93943-5502.  
E-mail: carolyn.reynolds@nrlmry.navy.mil

---

<sup>1</sup> Overview articles for the full TPARC and TCS-08 experiments are in preparation. Currently, information on the field program is available on the Earth Observing Laboratory (EOL) TPARC catalogue Web site ([http://catalog.eol.ucar.edu/tparc\\_2008/](http://catalog.eol.ucar.edu/tparc_2008/)).

Report Documentation Page			Form Approved OMB No. 0704-0188		
Public reporting burden for the collection of information is estimated to average 1 hour per response, including the time for reviewing instructions, searching existing data sources, gathering and maintaining the data needed, and completing and reviewing the collection of information. Send comments regarding this burden estimate or any other aspect of this collection of information, including suggestions for reducing this burden, to Washington Headquarters Services, Directorate for Information Operations and Reports, 1215 Jefferson Davis Highway, Suite 1204, Arlington VA 22202-4302. Respondents should be aware that notwithstanding any other provision of law, no person shall be subject to a penalty for failing to comply with a collection of information if it does not display a currently valid OMB control number.					
1. REPORT DATE <b>2010</b>	2. REPORT TYPE		3. DATES COVERED <b>00-00-2010 to 00-00-2010</b>		
4. TITLE AND SUBTITLE <b>Naval Research Laboratory Multiscale Targeting Guidance for T-PARC and TCS-08</b>			5a. CONTRACT NUMBER		
			5b. GRANT NUMBER		
			5c. PROGRAM ELEMENT NUMBER		
6. AUTHOR(S)			5d. PROJECT NUMBER		
			5e. TASK NUMBER		
			5f. WORK UNIT NUMBER		
7. PERFORMING ORGANIZATION NAME(S) AND ADDRESS(ES) <b>Marine Meteorology Division, Naval Research Laboratory, Monterey, CA</b>			8. PERFORMING ORGANIZATION REPORT NUMBER		
9. SPONSORING/MONITORING AGENCY NAME(S) AND ADDRESS(ES)			10. SPONSOR/MONITOR'S ACRONYM(S)		
			11. SPONSOR/MONITOR'S REPORT NUMBER(S)		
12. DISTRIBUTION/AVAILABILITY STATEMENT <b>Approved for public release; distribution unlimited</b>					
13. SUPPLEMENTARY NOTES					
14. ABSTRACT					
15. SUBJECT TERMS					
16. SECURITY CLASSIFICATION OF:			17. LIMITATION OF ABSTRACT <b>Same as Report (SAR)</b>	18. NUMBER OF PAGES <b>19</b>	19a. NAME OF RESPONSIBLE PERSON
a. REPORT <b>unclassified</b>	b. ABSTRACT <b>unclassified</b>	c. THIS PAGE <b>unclassified</b>			

different objectives during T-PARC/TCS-08, including process studies on TC formation and structure, TC extratropical transition, and satellite calibration and validation. The objective most relevant to the products described here was TC-targeted observations, where additional observations are taken in sensitive regions deemed most likely to have an impact (hopefully an improvement) on the TC forecast of interest [see the review article by Langland (2005) for more information on targeted observations]. Synoptic-scale surveillance flights in sensitive regions have been taken under ongoing programs for Atlantic storms (Aberson 2003) and in the western North Pacific for TCs threatening Taiwan (Wu et al. 2005, 2007b).

To support the field campaign, primarily the targeted observations objective but also some of the other objectives, the Naval Research Laboratory (NRL) produced real-time products based on global-scale and mesoscale forecast models and their adjoint systems. Adjoint allow for the calculation of the sensitivity of TC forecasts to changes in the initial state in a mathematically rigorous, computationally feasible manner. These products provided information on features and processes that influence the TC track and intensity forecasts and were used along with products from other institutions to determine resource allocations and deployments (such as when and where aircraft would take additional observations). NRL contributed both global-scale and mesoscale products, providing critical information on both large-scale remote influences and the sensitivity of the forecast to finescale structures within the storm itself. The T-PARC/TCS-08 field program represents the first time a mesoscale adjoint system has been used for tropical cyclone targeting guidance during the formation and early development stages. Section 2 describes the global-scale products and section 3 describes the mesoscale products. Section 4 provides a summary of the products and lessons learned. The purpose of this article is to describe the NRL products produced in real time to support this field program. Ongoing and follow-on research on process studies and data impact studies facilitated by the information collected during T-PARC/TCS-08 will be reported on in the future.

## 2. Global-scale products

Both singular vector products and ensemble products were produced in support of T-PARC/TCS-08 using the Navy Operational Global Atmospheric Prediction System (NOGAPS; Hogan and Rosmond 1991; Peng et al. 2004) in conjunction with the NRL Atmospheric Variational Data Assimilation System (NAVDAS; Daley and Barker 2001). The SV products are described first, followed by a brief description of some of the ensemble products.

### a. Singular vector formulation

The leading SVs represent the fastest-growing perturbations to a particular forecast (in a tangent linear sense) and, as such, have been used for ensemble design (e.g., Molteni et al. 1996; Puri et al. 2001) and adaptive observing applications (e.g., Langland et al. 1999; Majumdar et al. 2002). While the first applications were for midlatitude systems (e.g., Buizza and Montani 1999; Reynolds et al. 2001; Montani and Thorpe 2002), more recently SVs have been applied to tropical cyclones (Barkmeijer et al. 2001; Peng and Reynolds 2005, 2006; Peng et al. 2007), demonstrating their utility for TC ensembles and illustrating the impacts of both the remote and near-storm environments on tropical cyclone forecasts. Recent articles have made quantitative assessments of the similarities between singular-vector-based targeted observing products and other adjoint and ensemble-based targeting products for TCs in both the Atlantic (Majumdar et al. 2006; Reynolds et al. 2007) and Pacific (Wu et al. 2009). These studies indicated strong similarities between SV products from different models, but significant differences between SV products and ensemble-based products.

For linear perturbation growth, an initial perturbation  $\mathbf{p}_0$  can be propagated forward in time using the tangent forward propagator,  $\mathbf{L}$ , representing the equations of the nonlinear forecast model linearized about the nonlinear forecast trajectory, such that  $\mathbf{L}\mathbf{p}_0 = \mathbf{p}_r$ . Here,  $\mathbf{L}$  can be represented by its singular values and initial and final-time SVs as such:

$$\mathbf{L} = \mathbf{E}^{-1/2} \mathbf{U} \mathbf{D} \mathbf{V}^T \mathbf{E}^{1/2}, \quad (1)$$

where  $\mathbf{V}$  ( $\mathbf{U}$ ) are matrices with columns composed of the initial (final) SVs,  $\mathbf{v}_n$  ( $\mathbf{u}_n$ ), and  $\mathbf{D}$  is a diagonal matrix whose elements  $d_n$  are the singular values of  $\mathbf{L}$ . The superscript  $T$  denotes the transpose, and  $\mathbf{E}$  is the metric that defines how the perturbations are measured. The SVs form an  $\mathbf{E}$ -orthonormal set of vectors at the initial and final times. The SVs satisfy the eigenvector equation  $\mathbf{L}^T \mathbf{E} \mathbf{L} \mathbf{y}_n = d_n^2 \mathbf{E} \mathbf{y}_n$ , where  $\mathbf{y}_n = \mathbf{E}^{-1/2} \mathbf{v}_n$ , and  $d_n$  and  $\mathbf{v}_n$  are the  $n$ th singular value and initial-time SV, respectively. The leading SV maximizes the ratio of the final perturbation energy to the initial perturbation energy:

$$\frac{\langle \mathbf{L}\mathbf{p}_0; \mathbf{E}\mathbf{L}\mathbf{p}_0 \rangle}{\langle \mathbf{p}_0; \mathbf{E}\mathbf{p}_0 \rangle}, \quad (2)$$

where  $\langle \rangle$  represents a Euclidean inner product. The second SV maximizes this ratio under the constraint of being orthogonal to the first SV, the third SV maximizes this ratio under the constraint of being orthogonal to the first two SVs, and so on. For further discussion of SV

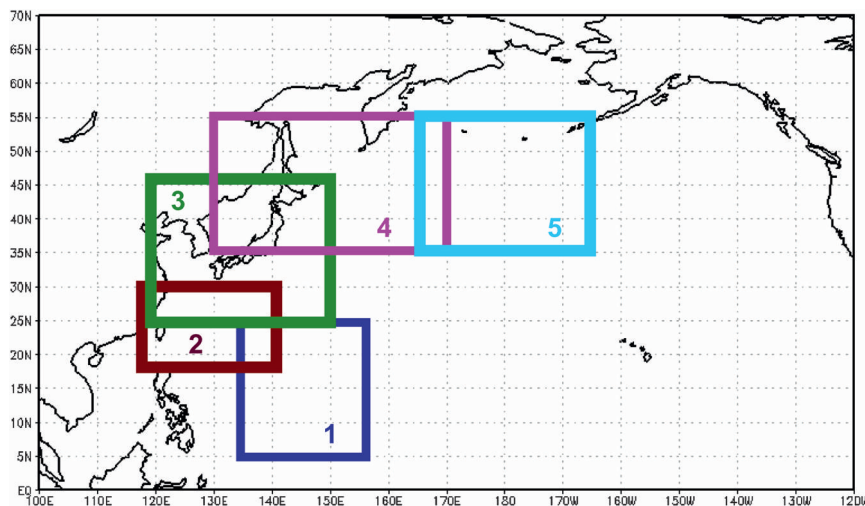


FIG. 1. The five fixed verification regions are denoted by rectangles: Guam (1), Taiwan (2), Japan (3), the ET (4), and the North Pacific (5).

diagnostics and their utility in atmospheric sciences, see Palmer et al. (1998) and references therein.

*b. Singular vector configuration for T-PARC/TCS-08*

The SVs are calculated using the tangent and adjoint models of NOGAPS with a total energy metric at both the initial and final times (Rosmond 1997). The SVs are calculated at a reduced resolution of T79L30, although the linearization is based on the trajectory from the full-physics, high-resolution (T239L30) operational NOGAPS forecast. Because the SVs are calculated at this relatively coarse (1.5°) resolution, they are used for guidance on the influence of synoptic- and large-scale features on the evolution of the TC forecast, rather than on the influence of the specific structure of the storm itself or other finescale features. A local projection operator (Buizza 1994) is employed to optimize the final-time perturbation energy in a particular verification region of interest. The vertically integrated energy corresponding to the first three leading SVs is used to construct an SV sensitivity pattern.<sup>2</sup> The SV sensitivity pattern,  $\mathbf{s}$ , is a composite of the vertically integrated total energy of the leading SVs, weighted by the singular values as such:

$$\mathbf{s} = \sum_{j=1}^3 \frac{d_j^2}{d_1^2} \mathbf{a}_j(\mathbf{b}, t), \quad (3)$$

where  $\mathbf{a}_j(\mathbf{b}, t)$  is the vertically integrated total energy of the  $j$ th SV at latitude–longitude grid location  $\mathbf{b}$ . The

<sup>2</sup> Note, this is not the same as adjoint sensitivity, although both patterns will highlight fast-growing structures (Gelaro et al. 1998).

forecast length over which the SVs are calculated is referred to as the optimization time. In addition, a “lead time” is built into the calculation to account for the time necessary to calculate the products, make decisions about targeting, and deploy the targeted platforms (usually aircraft). Typical lead times and optimization times would be 48–60 h. Thus, from a forecast started on 0000 UTC 1 August with a lead time of 48 h and an optimization time of 48 h, the SVs would be optimized over the 48–96-h portion of that forecast. The initial-time SVs would then be valid for targeted observations to be taken on 0000 UTC 3 August. These, theoretically, would have an impact on the forecast verifying 2 days later (0000 UTC 5 August) in the verification region defined by the local projection operator.

At NRL, NOGAPS SVs were produced for five fixed regions twice daily, from the 0000 and 1200 UTC operational forecasts. The five fixed areas included the Guam, Taiwan, and Japan regions, as well as an extratropical transition (ET) region and a central North Pacific region (Fig. 1). The first three regions correspond to the air bases of the targeted observing aircraft, and the later two were chosen to examine the sensitivity of the forecasts to TCs undergoing extratropical transition and their downstream impacts. The SVs for the TC targeting intercomparison papers (Majumdar et al. 2006; Reynolds et al. 2007; Wu et al. 2009) were calculated using the same software and framework except for the fact that storm-centered verification regions were used, as opposed to the fixed verification regions used here. Therefore, it was of interest here to examine the applicability of fixed verification regions for TC applications. Most of the TCs of interest during T-PARC/TCS-08 occurred in areas



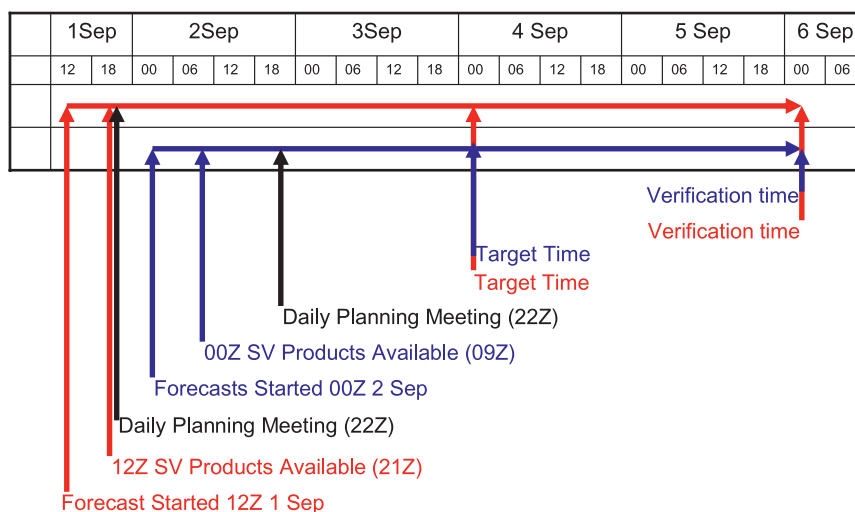


FIG. 2. Schematic of timeline for SV calculations for a forecast started from 1200 UTC 1 Sep (red horizontal line) and a forecast started from 0000 UTC 2 Sep (blue horizontal line). Red text and arrows indicate the forecast start times, the times the SV products are available, the target times, and the verification times. The times of the daily planning meeting on 1 and 2 Sep are also included.

covered by at least one of these regions. The lead times and optimization times for all the fixed regions from the 0000 UTC forecast were 48 h. For products from the 1200 UTC forecast, the lead times were 60 h. In this way, the products produced from both the 0000 and 1200 UTC runs were for targets centered on 0000 UTC, when many (but not all) of the targeted observing flights took place. A timeline is given in the schematic in Fig. 2. For example, the Taiwan SVs off the 1200 UTC run on 1 September with a 60-h lead time and 48-h optimization time produced targets valid for 0000 UTC 4 September with the forecast verification time of 0000 UTC 6 September. These products became available at about 2100 UTC on 1 September, enabling a “first look” at targets valid 0000 UTC 4 September, just prior to the T-PARC daily planning meetings that took place at 2200 UTC. The next morning, products off the 0000 UTC run on 2 September (available around 0900 UTC 2 September), with a 48-h lead time and a 48-h optimization time, became available for the same target times and verification times as the 60-h lead targets off the 1200 UTC run from the previous day. The 0000 UTC products provided presumably more accurate target information, as the lead time was reduced from 60 to 48 h, and shorter forecasts are, on average, more skillful. This allowed for the refinement of deployment plans as was appropriate.

Ideally, the adaptive observing technique would take into consideration the data assimilation system and the routine observations, as well as additional observations that would be taken before the target time. If the inverse

of the true analysis error covariance is used as the initial-time metric, then the final-time SVs will be the leading eigenvectors of the forecast error covariance (Ehrendorfer and Tribbia 1997). Consideration of the analysis error can be incorporated through the use of different initial-time metrics as in Hessian SVs (Barkmeijer et al. 1999; Leutbecher et al. 2002) or variance SVs (Gelaro et al. 2002; Reynolds et al. 2005). Reynolds et al. (2007) show that for variance SVs applied to Atlantic hurricanes, the results are quite sensitive to the estimate of the analysis error variance used. Because of the uncertainty associated with current analysis error variance estimates, and to facilitate comparison with SV calculations from other centers, the SVs for this field project were calculated using a total energy metric at both the initial and final times. Expected spatial variations in analysis error were considered subjectively. Future experimentation will include SVs constrained by different estimates of analysis error variance. Ideally, one could include quantitative estimates of the impacts of additional observations on the analysis and forecast through incorporation of the observation sensitivity, which uses the adjoints of both the forecast model and the data assimilation system (e.g., Langland and Baker 2004).

The appropriateness of the linearity assumption for TC SVs for 48-h optimization times has been investigated by Peng and Reynolds (2006) and Reynolds et al. (2009). They found that the structures of evolved SV-based nonlinear perturbations are similar to the final-time SVs, and also found that the day-to-day variations in

the nonlinear growth of SV-based perturbations are well reflected by the linear estimates. Therefore, a 48-h optimization time is appropriate for the coarse-resolution dry NOGAPS SV calculations. The linearity assumption breaks down sooner for the Coupled Ocean–Atmosphere Mesoscale Prediction System (COAMPS) high-resolution moist calculations, leading to the adoption of shorter optimization times for the COAMPS calculations, as discussed in section 3. While the long lead times of 48 and 60 h were necessary to allow for the planning and deployment processes, additional SVs with shorter (24 and 36 h) lead times were calculated during high interest periods. The SVs based on the shorter and presumably more accurate forecasts allowed for refinement of the targeting plans as appropriate.

The SVs were calculated on an IBM P5 at the Department of Defense/Naval Oceanographic Office's (DoD/NAVO) Supercomputer Resource Center at the Stennis Space Center in Mississippi, under the DoD High Performance Computing (HPC) Program using the operational forecast trajectory that was transferred there from the Fleet Numerical Meteorology and Oceanography Center in Monterey, California. From the Stennis Space Center, graphical products were sent to several different sites, including the NRL T-PARC/TCS-08 Web site, the National Center for Atmospheric Research's Earth Observing Laboratory catalogue, and the European Centre for Medium-Range Weather Forecasts–Met Office (ECMWF–UKMO) “Preview” Web site. The Preview Web site included products from several different organizations (including SVs from ECMWF, and ensemble transform Kalman filter products from UKMO and University of Miami–National Centers for Environmental Prediction) and displayed these products in a uniform manner, facilitating intercomparison. Other products available, though not necessarily on the Preview site, included SVs from the University of Yonsei in Korea and the Japan Meteorological Agency, adjoint-derived sensitivity steering vectors from National Taiwan University (Wu et al. 2007a), ensemble-based sensitivity from the University of Washington, and COAMPS adjoint sensitivities from NRL (described in section 3). Consensus among a variety of products was looked for in determining priority regions for targeted observations.

### c. Examples of real-time SV products

The vertically integrated total energy of the SVs was displayed along with 500-hPa streamfunction and 850-hPa positive vorticity. These fields were useful for identifying the features of the flow that the sensitivity was associated with at both initial (target) and final (verification) times. As an example, Fig. 3a shows the NOGAPS

SV initial-time sensitivity (shaded) for TC Jangmi at 0000 UTC 28 September 2008, as identified by the concentric 850-hPa vorticity contours at 22°N, 123°E. Figure 3a indicates that the 48-h forecast of TC Jangmi is sensitive to changes in the peripheral anticyclonic flow, centered at 13°N, 127°E, to the southeast of the TC, as well as a weakness in the anticyclonic flow to the north of the TC, as shown in the 500-hPa streamlines. The importance of both these features for influencing TC motion has been previously suggested through simple dynamical studies as well as complex numerical integrations (e.g., Carr and Elsberry 1995). At the final (verification) time (0000 UTC 30 September; see Fig. 3b), the total energy field of the SV sensitivity has two maxima centered on TC Jangmi (now at 25°N, 118°E). The SV vorticity pattern (not shown) exhibits a plus-minus dipole about the center, indicating that the singular vector perturbation would result in a shift in the position of Jangmi, primarily in the southwest–northeast direction. If analysis error projected onto these initial SVs, and the perturbation growth was approximately linear, this would indicate potential forecast uncertainty in the position of Jangmi in the northeast–southwest direction.

In this case, the TC is near the western edge of the Taiwan verification region, as indicated by the red box in Fig. 3b. To explore the impacts of using fixed verification regions, the SV calculations are rerun for the same case, but with a verification region centered on the forecast position of the storm (Fig. 3c). Comparison of Figs. 3c and 3a indicates that the SV patterns are similar overall, although there are some differences, such as a reduced emphasis on the peripheral high to the southeast for the storm-centered verification region. The final-time SVs for the storm-centered verification region (not shown) are almost indistinguishable from those for the Taiwan verification region, shown in Fig. 3b. An additional piece of information available from the SV calculation is the amplification factor associated with each of the SVs. These values represent the factor by which the total energy of an initial SV perturbation would increase over the optimization period for linear perturbation growth. The amplification factors (squared singular values) for the Taiwan SVs were 33.0, 13.3, and 11.6, and for the storm-centered SVs were 32.9, 11.1, and 7.1; that is, they were almost identical for the leading SV, but smaller for the storm-centered verification region for the second and third SVs. The similarities between the fixed and storm-centered SVs support the idea that if the final-time SVs are centered on the storm of interest, the initial-time SVs are relevant, even if the storm was not centered in the fixed verification region.

There were occasions, however, where inspection of the final-time SVs indicated that they were not associated

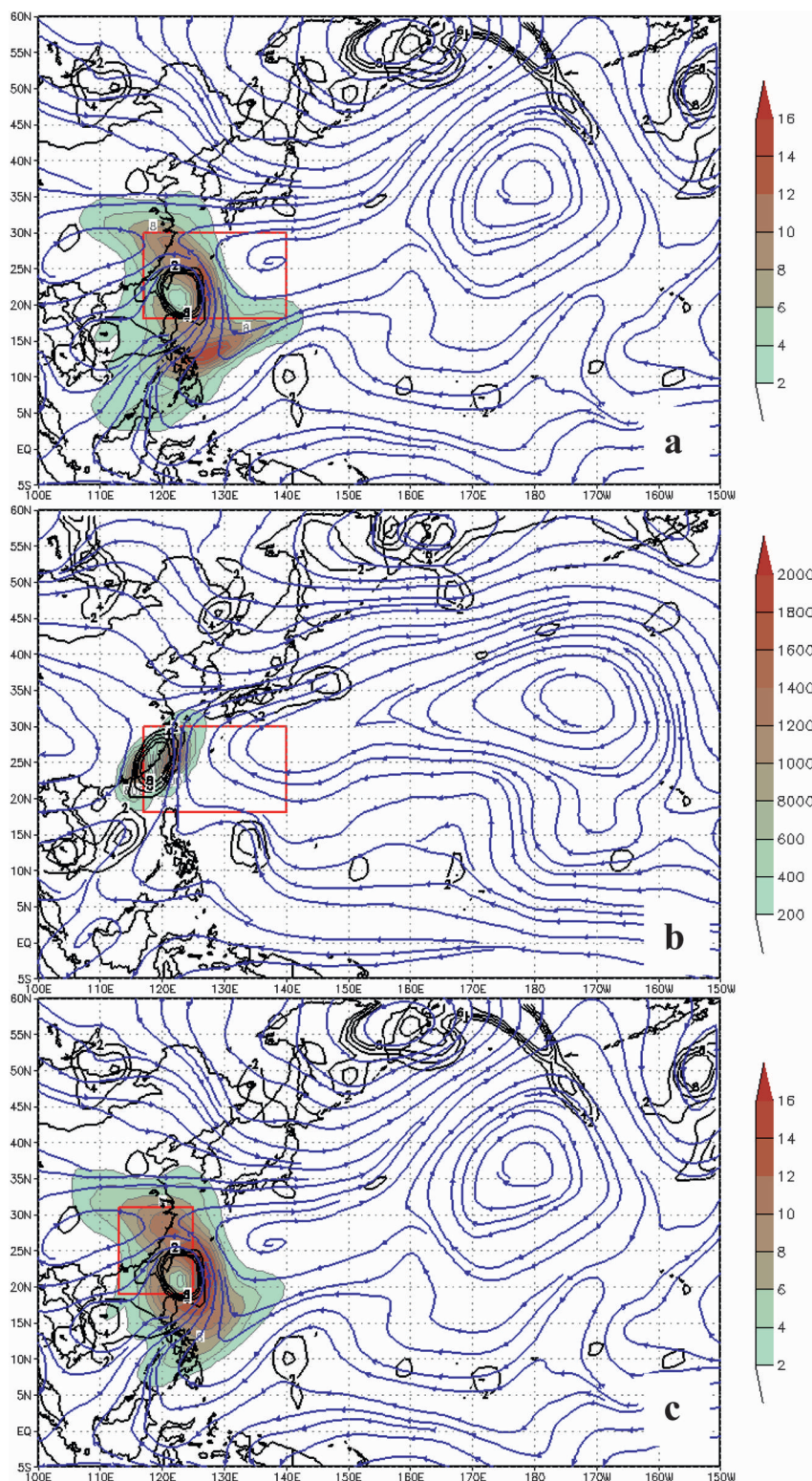


FIG. 3. Vertically integrated SV sensitivity (shaded, values in  $\text{J kg}^{-1}$  given in color bar) for the Taiwan region for (a) targets valid at 0000 UTC 28 Sep 2008 and (b) verification at 0000 UTC 30 Sep 2008. NOGAPS 500-hPa streamlines given in blue and 850-hPa vorticity at  $2, 4, 6$ , and  $8 \times 10^{-5} \text{ s}^{-1}$  given by the black contours. The Taiwan verification region is outlined by the red box. (c) As in (a) except that the SVs are based on a storm-centered verification region, rather than the Taiwan region.



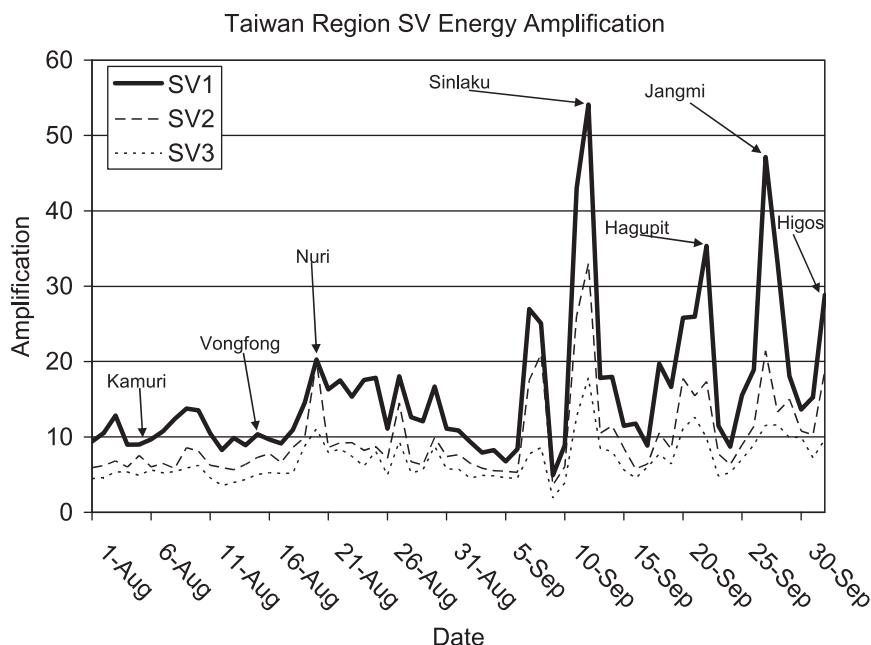


FIG. 4. The 48-h total energy amplifications of Taiwan regions SV1 (thick solid), SV2 (thin dashed), and SV3 (thin dotted), for initial-time SVs valid on the dates given (from 1 Aug through 2 Oct). The names of TCs that existed within the Taiwan verification region and the peak SV amplification associated with the TCs are noted.

with the TC of interest, and therefore the initial SVs were not appropriate TC targets in these cases. In 18 out of 88 cases (considering SVs calculated from 18 August through 30 September off the 0000 and 1200 UTC runs) at least one of the three leading SVs, for at least one of the five fixed verification regions, was not associated with the feature of interest. This was more common for the more northerly fixed verification regions, where a TC and an independent trough might both exist in the verification region, and certain SVs were associated with the TC, and others with the trough. With fixed verification regions (as opposed to those that would always be centered on the feature of interest), it was therefore necessary to inspect the final-time SVs to make sure that the initial (target) time SVs were associated with the TC of interest.

Figure 4 shows the time series of the total energy amplification factor for the three leading SVs for the Taiwan verification region for the entire field-phase period. These values show significant day-to-day variability and are considerably larger on average during September than during August, reflecting relatively active and quiet periods, respectively. The TCs that occurred during the field phase within the Taiwan verification region, and maximum amplification factors associated with these storms, are also indicated in Fig. 4. The first two storms, Kamuri and Vonfong, were both weak systems that formed in the far southwest and northeast corners of the Taiwan

verification region, respectively, and quickly moved out of the verification region and, thus, had no significant signal in the SVs. The other TCs (Nuri, Sinlaku, Hagupit, Jangmi, and Higos) were all associated with relative peaks in the amplification factors, reflecting the relatively large potential for perturbation growth during periods when TCs were in the verification region. This potential for larger perturbation growth may be only loosely related to low predictability or large forecast uncertainty because forecast errors will be influenced by the specific projection of the analysis error onto the singular vector structures. This projection, as well as the validity of the tangent linear assumption, will vary from case to case.

In addition to the vertically integrated SV sensitivity, information was also available on the vertical distribution of the SV sensitivity, displayed through sensitivity summary plots for the temperature and vorticity components (Fig. 5). These plots indicate with numbers and colors the regions where the SV potential energy and rotational kinetic energy were greater than 70% of the maximum total energy value. The numbers correspond to the SV number (1–3), and the colors correspond to the atmospheric layer (blue above 400 hPa, green between 400 and 700 hPa, and gold below 700 hPa). These types of plots were first developed and used at ECMWF (e.g., Montani et al. 1999) and NRL (e.g., Gelaro et al. 1999) in support of midlatitude targeting programs such

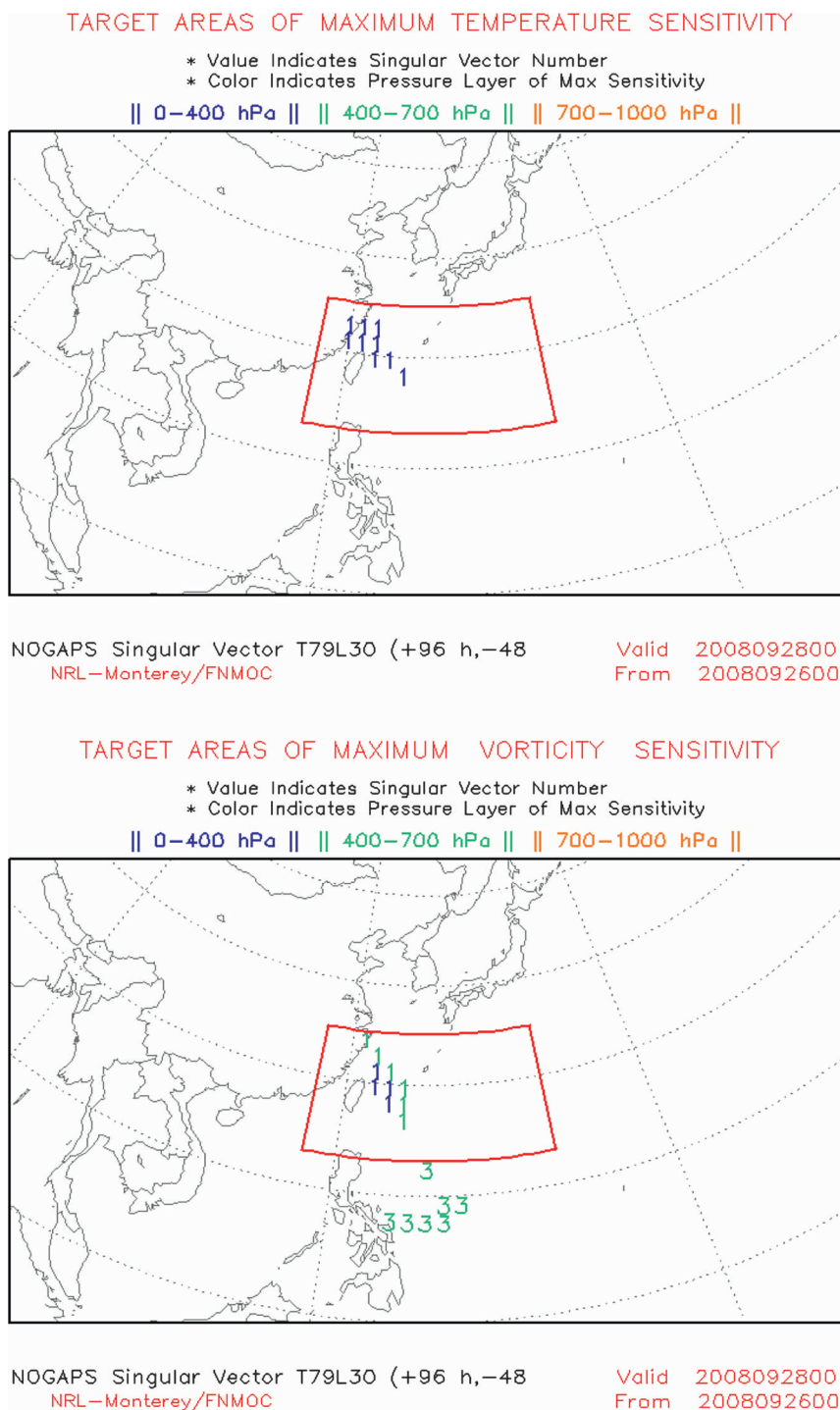


FIG. 5. Products showing the locations of the (top) maximum temperature and (bottom) vorticity sensitivities for the first three SVs. The number refers to the SV number (1–3), and the color indicates the altitude layer (above 400 hPa is blue, 400–700 hPa is green, and below 700 hPa is gold). The Taiwan verification region is outlined by the red box.

as the Fronts and Atlantic Storm-Track Experiment (FASTEX; Palmer et al. 1998; Langland et al. 1999; Buizza and Montani 1999). The plots shown in Fig. 5 correspond to the same SV sensitivities for TC Jangmi as shown in Fig. 3. These summary plots show that to the north of the storm, in the area of weakness between the two anticyclones north of Taiwan, the sensitivity is primarily in the upper-level temperature and mid- and upper-level vorticity from SV1. The temperature and vorticity sensitivities collocated with the weakness in the subtropical high suggest that the TC evolution will be sensitive to changes in this feature, which can be impacted by both mass and wind field initial perturbations. The sensitivity to the southeast of the TC is primarily in the midlevel vorticity from SV3 in the vicinity of the peripheral high east of the Philippines (no targets from SV2 were above the plotting threshold limit). This information was useful in determining what types of data at what altitudes would be most likely to impact the forecast.

The small number of TCs that occurred during the 2008 field program (four TCs were targeted) prevents us from making generalizations about the characteristics of the SV sensitivity patterns for different types of storms or different periods in the storm life cycle. However, the SV characteristics for 2008 were generally consistent with characteristics of SVs computed for the western North Pacific TCs for the 2006 season, as described in detail in Reynolds et al. (2009) and Chen et al. (2009). The large sample size (18 storms, 72 forecasts) of the 2006 season allowed for a systematic investigation of the characteristics of the TC SVs as a function of track characteristics and life cycle. For example, Reynolds et al. (2009) grouped the storms into straight-moving and recurving categories. Composites about the storm centers for these two categories showed an annulus about the storm center for the straight-moving group, consistent with the results of Peng and Reynolds (2006), and enhanced sensitivity to the northwest for the recurving storms. An example of a typical recurving TC life cycle shown in Reynolds et al. (2009) illustrates how its sensitivity is centered around the storm before recurvature, and is gradually enhanced to the northwest of the storm, in the vicinity of an approaching trough, as the storm begins to recurve. Chen et al. (2009) find, through compositing techniques, strong sensitivity in the regions of confluence between different features of influence, very similar to the sensitivity shown in Fig. 3a in the confluence region between the two anticyclonic circulations to the north of the storm.

The NOGAPS SVs were used in conjunction with the targeted observing guidance from several other institutions in deciding where and/or when additional resources (such as targeting flights and off-time radiosondes) would

be deployed. This was accomplished through an examination of all the different targeting products available to establish a consensus among the products. In addition, ensemble products were used to examine the forecast uncertainty in the tropical cyclone tracks and the features of interest in the sensitive regions. Deployment plans would also be modified or limited by consideration of air-traffic control issues, the routine observing network, and deployment of other special observations (such as off-time radiosondes or the deployment of other aircraft).

#### *d. Ensemble products*

In addition to the SV products described above, NOGAPS ensembles were also produced on a real-time basis in support of T-PARC/TCS-08. These 32-member 10-day ensembles were run at a T119L30 resolution and produced using the ensemble transform initial perturbation scheme, described in McLay et al. (2008). The ensembles were run once a day off the 0000 UTC analysis. These ensembles did not account for model error, and as such tended to be underdispersive in the tropics. They therefore underestimated the uncertainty of the TC tracks in the tropics and subtropics. (A study of the genesis and track prediction using ensembles run after the field program that include model uncertainty in the form of stochastic convection is currently under way.) However, there was some utility for the ensemble products, particularly concerning the potential downstream impacts of tropical cyclones as they underwent extratropical transition. Jones et al. (2003) show that periods of extratropical transition may be associated with significant drops in forecast skill on a hemispheric basis. Cardinali et al. (2007) show that the impacts of SV-based adaptive (targeted) observations over the North Atlantic are almost 4 times higher during extratropical transitions of TCs than the impacts averaged for all cases. Harr et al. (2008) and Anwender et al. (2008) have shown plumes of large forecast uncertainty, represented by ensemble spread, emanating downstream from extratropical transitions. Following their work, time-longitude plots of the NOGAPS ensemble spread were produced on a daily basis. Figure 6 gives an example from 0000 UTC 19 September of large ensemble spread emanating downstream from the region where TC Sinlaku enters the midlatitudes (the longitude of the TC as it recurves into the midlatitudes is indicated by the black squares). Figure 6a shows the ensemble standard deviation about the ensemble mean of the 200-hPa meridional wind (shaded), along with contours of the 200-hPa meridional wind from the control member. Figure 6b shows this field divided by the ensemble standard deviation averaged over the month of September, indicating regions of ensemble standard deviation that were 30%–50% larger



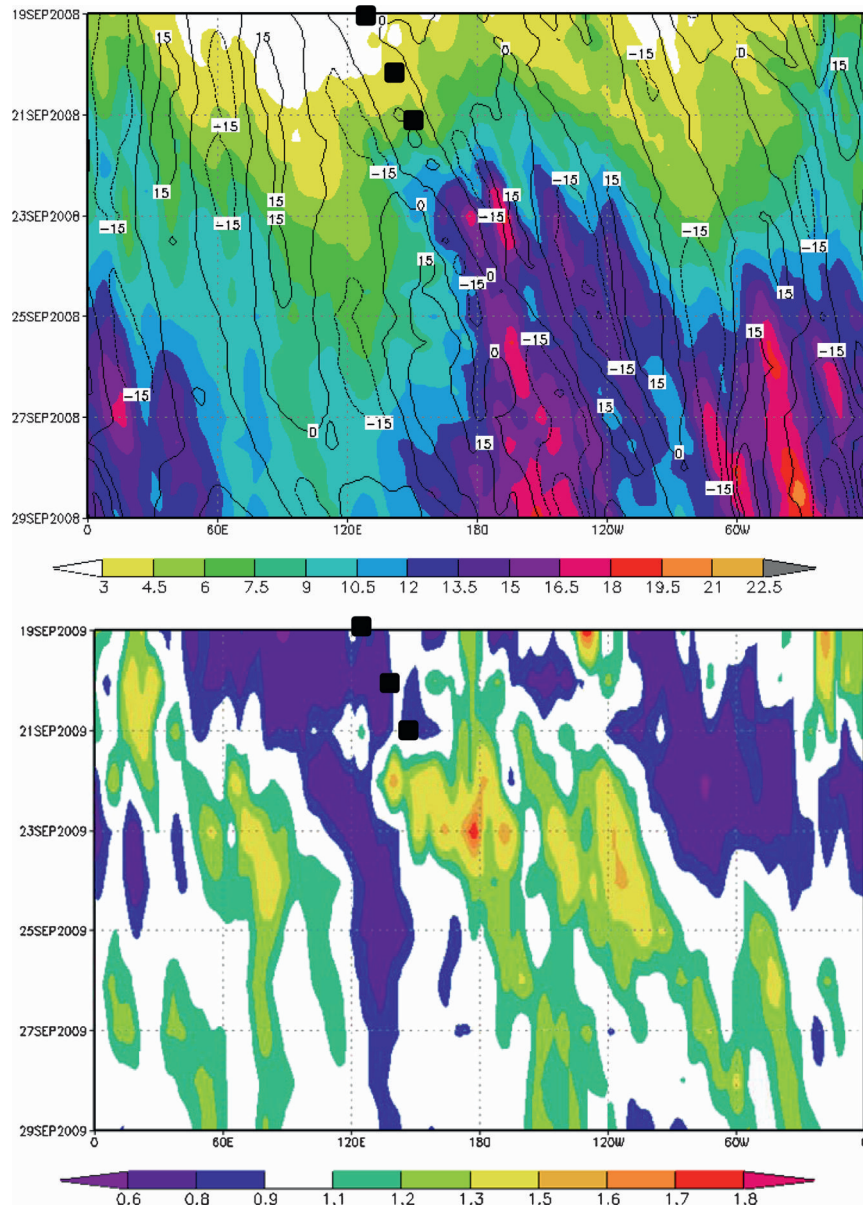


FIG. 6. (top) The 200-hPa meridional wind of the control (no initial perturbation) ensemble member ( $\text{m s}^{-1}$ , black contours) and the ensemble standard deviation ( $\text{m s}^{-1}$ , values given in color bar), averaged from  $35^{\circ}$  to  $60^{\circ}\text{N}$  as a function of longitude. Results are for a 10-day ensemble forecast starting at 0000 UTC 19 Sep, with time increasing downward. (bottom) The same ensemble standard deviation divided by the ensemble standard deviation averaged over the month of September. Black squares indicate the longitude of TC Sinlaku as it recurves into the midlatitudes.

than the average values emanating downstream from the TC as it enters the midlatitudes. Inspection of these plots from the forecasts started days prior and after this example indicates enhanced ensemble standard deviations at later and earlier forecast times, respectively, corresponding to when extratropical transition occurred in the forecasts. This indicates that the forecast uncertainty is associated

with the event of the extratropical transition, and is not just a function of forecast lead time. This large ensemble spread is a reflection of the complexity of the interactions between the tropical cyclone and the midlatitude jets and the subsequent downstream impacts (e.g., Harr et al. 2000).

In addition, several ensemble “spaghetti plots,” as well as probabilistic plots for low-shear and high vorticity

conductive to tropical cyclone genesis, were also produced (not shown). Spaghetti plots from different institutions were used to aid in estimating the uncertainty in the features highlighted by the sensitivity guidance.

### 3. Mesoscale products

Products from the newly developed COAMPS forecasting system designed specifically for TCs are first briefly described, followed by a description of the targeting guidance produced using the COAMPS adjoint.

#### *a. COAMPS-TC background and forecasts*

A new version of COAMPS (Hodur 1997; Hodur and Doyle 1998) has been developed specifically for forecasting tropical cyclones and is referred to as COAMPS-TC. The COAMPS-TC system is composed of data quality control, analysis, initialization, and forecast model subcomponents. NAVDAS is the data assimilation system for both NOGAPS and COAMPS. In NAVDAS, the wind observations are obtained from radiosondes, dropsondes, pibals, aircraft, satellites, and surface measurements. Temperatures are obtained from radiosondes, dropsondes, Defense Meteorological Satellite Program (DMSP), and National Oceanic and Atmospheric Administration (NOAA) satellites, ships, buoys, and aircraft. Enhancements to the NAVDAS system for COAMPS-TC include the addition of synthetic observations that define the TC structure and intensity. Also, as part of the TC analysis procedure, the preexisting TC circulation in the COAMPS-TC first-guess fields is relocated based on the Joint Typhoon Warning Center (JTWC) warning message to allow for an accurate representation of the TC position during the NAVDAS analysis. Following the analysis, the analyzed fields are initialized to reduce the generation of spurious, high-frequency waves. One balance that is imposed in COAMPS-TC currently is a hydrostatic balance on the analyzed temperature and pressure increments. This balance is accomplished through a variational method. An optional initialization based on a digital filter can be used to mitigate high-frequency oscillations during the early portion of the forecast.

The COAMPS-TC atmospheric model uses the non-hydrostatic and compressible forms of the dynamics following Klemp and Wilhelmson (1978). The model has prognostic variables for the  $u$ ,  $v$ , and  $w$  components of the wind; the perturbation Exner function; potential temperature; water vapor; cloud droplets; raindrops; ice crystals; snowflakes; graupel; aerosols; and turbulent kinetic energy (TKE), using a terrain-following height coordinate; and a horizontally staggered C grid. Explicit

moist physics (Rutledge and Hobbs 1983) is used to represent clouds and precipitation processes, while cumulus parameterization (Kain and Fritsch 1990; Kain 1993) is used for subgrid-scale convection at coarser resolutions. The 1.5-order TKE prediction scheme follows Deardorff (1980) using a level 2 Mellor and Yamada (1974) parameterization. The Harshvardhan et al. (1987) radiation scheme is used as well. The COAMPS atmospheric model can utilize any arbitrary number of nested grids, with a reduction ratio of 3:1 in grid spacing between the grids. The COAMPS-TC system contains special options for moving nested grids that follow the tropical cyclone centers. Additionally, the COAMPS-TC model contains representations of the sea spray processes and dissipative heating near the ocean surface, which may be necessary to obtain realistic tropical cyclone intensity forecasts.

The atmospheric module of the COAMPS-TC system was demonstrated in real time using horizontally nested grids with resolutions of 45, 15, and 5 km in support of T-PARC/TCS-08. The 15- and 5-km resolution meshes track the TC centers, which enabled the TC convection to be explicitly resolved on the finest mesh in an efficient manner. Lateral boundary conditions were provided from the operational NOGAPS T239L30 forecasts. The real-time COAMPS-TC system was run on an SGI Altix 4700 system with 9216 processors (18 nodes with 512 processors per node) at the Air Force Research Laboratory (AFRL) with support from the DoD High Performance Computing Program. Each run of COAMPS-TC utilized 64 of the SGI Altix processors. The mission plans for the research aircraft were based on forecasts derived from a number of models including COAMPS-TC. Some of these missions, particularly for the P3, were observational missions related to the TC structure. The forecasts of the TC structure and intensity from this new generation of models, such as COAMPS-TC, were used in developing the observational strategies for each mission.

An example of a real-time COAMPS-TC forecast initialized on 26 September 2008 performed in support of T-PARC/TCS-08 objectives is shown in Fig. 7. The forecast and best-track positions shown in Fig. 7a indicate a skillful forecast of the track of Supertyphoon Jangmi. The model-forecasted radar reflectivity (Fig. 7b) indicates a well-developed convective eyewall structure in the 5-km-resolution grid along with spiral rainbands. The forecast structure of the spiral rainbands is in general agreement with the Tropical Rainfall Measuring Mission (TRMM) 85-GHz imagery shown in Fig. 8 valid at 1856 UTC 27 September (approximately 5 h prior to the forecast shown in Fig. 7b). For example, the prominent rainband along the eastern flank of the tropical cyclone is well represented. However, the model did not

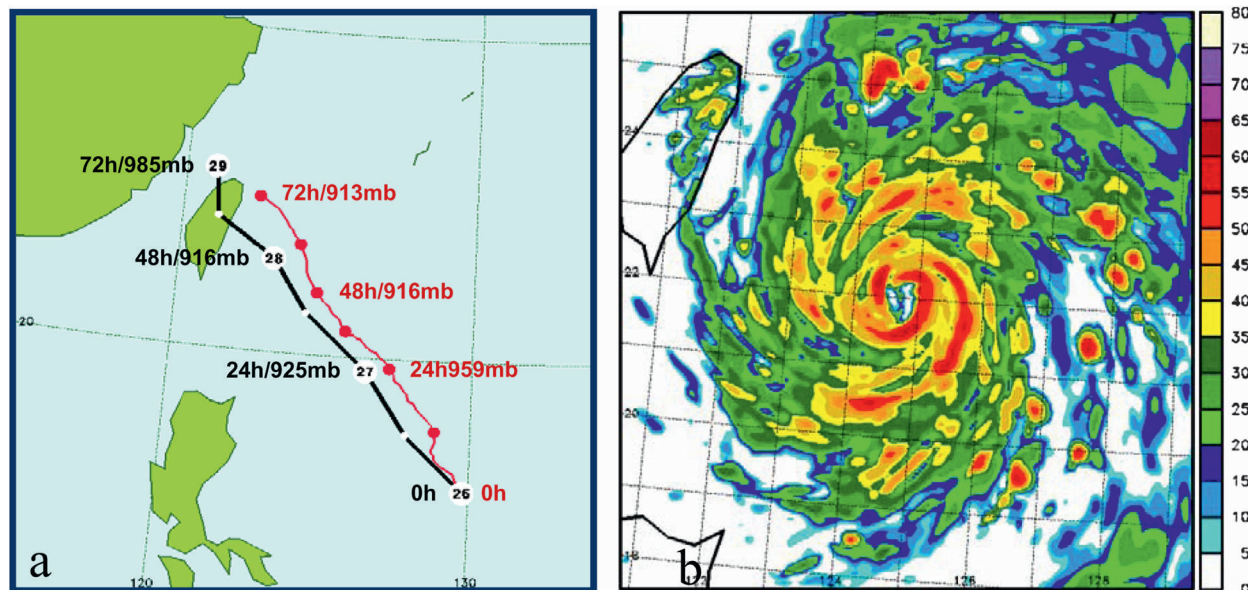


FIG. 7. COAMPS-TC real-time forecast initialized at 0000 UTC 26 Sep 2008 for Supertyphoon Jangmi. (a) The 72-h forecast tropical cyclone track (red) and best track (black), along with the estimated central pressure and model-predicted central pressure. The dots represent the tropical cyclone position at a 12-h interval. The larger white circles in the best track indicate the 0000 UTC position with the date denoted in the circle. (b) The model-forecasted radar reflectivity at 2 km (dBZ) valid at 0000 UTC 28 Sep (48 h) for the 5-km mesh.

capture the finescale double-eyewall structure at this time; it is uncertain that any of these finescale features are predictable on these time scales.

An analysis of the TC track performance during T-PARC/TCS-08 indicates that the COAMPS-TC track error was an improvement over the operational version of COAMPS for the western Pacific (COAMPS-WPAC) and comparable to or better than NOGAPS (particularly for the 36–48-h times) and a baseline forecast derived from a combination of climatology and persistence (CLIPER), as shown in Fig. 9. The track verification statistics were performed using a homogeneous sample. The number of cases for the verification ranges from 78 at the initial time to 48 at the final time. The statistical significance of the differences between the model scores, accounting for a 30-h serial correlation, has been calculated, and the difference between COAMPS-TC and CLIPER is found to be significant at the 92% and 95% levels at 36 and 48 h, respectively. (Differences at other forecast times were not statistically significant above the 90% level.) The difference between COAMPS-TC and COAMPS-WPAC is significant at the 94% level at 48 h. It should be noted that the operational COAMPS-WPAC has a horizontal resolution of 27 km and has not been used for operational prediction of tropical cyclones. A more detailed description of the COAMPS-TC design and statistical track and intensity verification will be reported upon in the future.

#### b. COAMPS adjoint

The tangent linear and adjoint COAMPS models were developed through the use of an automatic generator (Giering and Kaminski 1998) along with hand

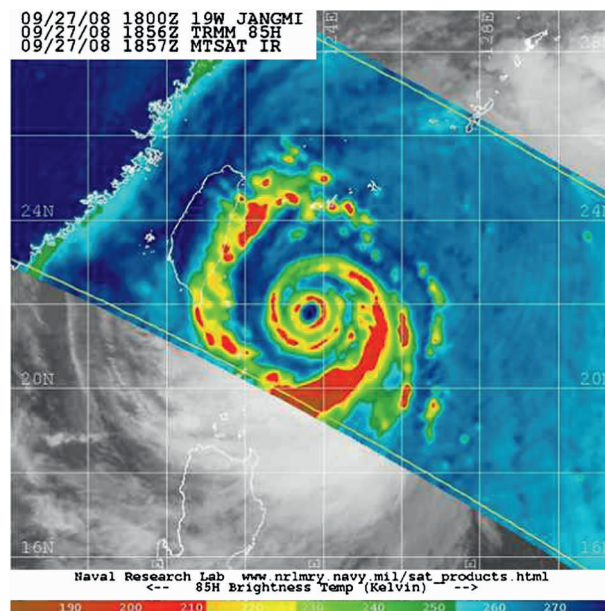


FIG. 8. TRMM 85-GHz and Multifunctional Transport Satellite (MTSAT) IR imagery for Jangmi valid at 1856 UTC 27 Sep with the color shading corresponding to the 85-GHz brightness temperature (scale in K).



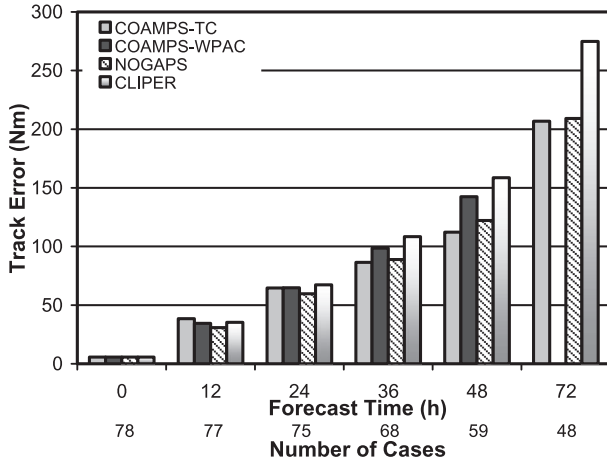


FIG. 9. The track error statistics for COAMPS-TC, COAMPS-WPAC, NOGAPS, and CLIPER. The COAMPS-WPAC is the current U.S. Navy operational model in the western Pacific.

coding (Amerault et al. 2008). In addition to the dynamical core, the tangent linear and adjoint models include the respective components of the turbulent kinetic energy, convective, and explicit moist physics parameterizations. The nonlinear model's trajectory is saved at an arbitrary number of time steps for use by the adjoint model and the switches that determine the discontinuities are the same in the nonlinear, tangent linear, and adjoint models (Zou et al. 1993; Vukicevic and Errico 1993). Following Mahfouf (1999), the perturbations to the vertical diffusion are neglected in the adjoint and tangent linear models, and the turbulent kinetic energy is derived from the nonlinear trajectory. By neglecting the perturbation to the vertical diffusion, we increase the stability of the mixing in the tangent linear model and avoid the occasional spurious behavior of the turbulent kinetic energy.

The adjoint model is used to create optimal perturbations (Errico and Raeder 1999) for the nonlinear and tangent linear models. Perturbations to a scalar measure  $J$  of the forecast are given as

$$J' = \sum_j \frac{\partial J}{\partial x_j} x'_j, \quad (4)$$

where  $\partial J / \partial x_j$  is the gradient (supplied by the adjoint model) of the scalar measure (known as a response function) with respect to the  $j$ th component of the initial condition. The  $j$ th component of the perturbation vector  $\mathbf{x}'$  is optimal (Rabier et al. 1996; Oortwijn and Barkmeijer 1995) if it is defined as

$$x'_j = \frac{s}{w_j} \frac{\partial J}{\partial x_j}, \quad (5)$$

for a weighting  $w_j$ . The solution in (5) was obtained by imposing the constraint

$$I = \sum_j w_j x'^2_j, \quad (6)$$

and the scaling parameter  $s$  is determined by applying (5) and (6) to obtain

$$s = \sqrt{2I} \left[ \sum_j \frac{1}{w_j} \left( \frac{\partial J}{\partial x_j} \right)^2 \right]^{-1/2}. \quad (7)$$

The weightings are calculated using the largest forecast difference on each vertical level  $k$  and for each variable  $m$ :

$$w_j = \frac{1}{[\max(|x^{m,k}_{t_r} - x^{m,k}_{t_0}|)]^2}, \quad (8)$$

where  $t_0$  is the initial time and  $t_r$  is the time when the optimal perturbations are calculated. The weightings only differ by variable and vertical level and have the same units as the inverse of the square of their respective fields. The scaling  $s$  has the same units of  $\text{joules}^{-1}$  and is chosen so that the largest perturbation of either the zonal wind speed or potential temperature is  $1.0 \text{ m s}^{-1}$  or  $1 \text{ K}$ , respectively. In this application of the adjoint and tangent linear models, the perturbations are calculated for the zonal ( $u$ ) and vertical ( $w$ ) wind speed components, potential temperature ( $\theta$ ), Exner pressure perturbation, water vapor, and the concentrations of cloud water and rainwater. The response function for the adjoint calculations is specified as the total kinetic energy,  $\frac{1}{2}(u^2 + v^2 + w^2)$ , which is applied over a rectangular box that extends over a  $1200 \times 1200 \text{ km}^2$  ( $30 \times 30$  grid cells) region and  $1 \text{ km}$  in the vertical above the surface (5 grid cells in the model vertical coordinate system).

Prior to T-PARC/TCS-08, experiments were performed that demonstrated that the tangent linear approximation is valid for tropical cyclone cases for integration times of  $24 \text{ h}$  and resolutions of  $40 \text{ km}$ . To assess the accuracy of the tangent linear approximation, comparisons have been performed using scaled adjoint perturbations of maximum amplitude  $1 \text{ m s}^{-1}$  or  $1 \text{ K}$  at the initial adjoint time. The perturbations are then evolved in the tangent linear and nonlinear models. The correlation between the tangent linear and nonlinear model-evolved  $u$ -wind component perturbation for mature storms and formation cases was found to be typically  $0.4$ – $0.8$ . Additionally, the evolved perturbation component patterns were compared visually and found to be generally similar for the tangent linear and nonlinear models, further confirming the validity of the tangent

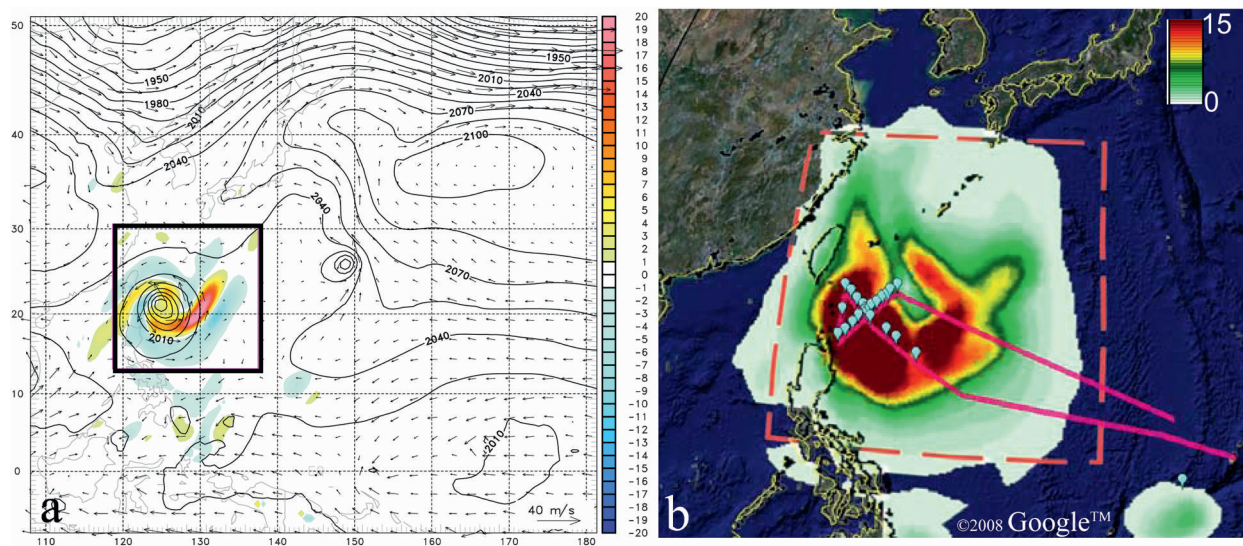


FIG. 10. The COAMPS (a) adjoint sensitivity fields for the 800-hPa vorticity ( $10^{-5} \text{ m}^2 \text{ s}^{-1}$ ) (color shading) and forward model 800-hPa geopotential heights (isopleths every 10 m) and wind vectors, and (b) vertically integrated total energy ( $\text{J kg}^{-1}$ ) based on the adjoint optimal perturbations valid at 1200 UTC 10 Sep 2008 for Typhoon Sinlaku using a 36-h lead time. The C130 flight track is shown by the solid magenta line and the dropsonde deployment locations are represented by the turquoise balloon symbols in (b). The boxes in (a) (black) and (b) (red dashed) indicate the regions over which the response function is applied. [Image in (b) was created using Google Earth.]

linear assumption for these time scales and resolutions. For forecast times longer than 24 h, the correlations decrease, particularly beyond 36 h. These experiments indicate that the adjoint model provides useful gradients for sensitivity analysis for optimization times of up to 24 h when the tangent linear model is valid.

### c. COAMPS adjoint sensitivity products

Mesoscale targeted observing products were produced using the COAMPS forecast and adjoint system twice daily, centered on storms of interest, at 40-km resolution. The adjoint system was run on an IBM P5 at the NAVO HPC facility. These products were produced with 24-, 36- and 48-h lead times. An adaptive response function region was used to target favorable areas for tropical cyclone formation and development. The response function was repositioned every forecast based on the expected region of interest and the potential for targeted observations. The adjoint-based products were disseminated on the World Wide Web via NRL and the T-PARC/TCS-08 Web sites.

Results indicate that forecasts of western Pacific tropical cyclones during both the formation and mature stages are very sensitive to the initial state given the rapid growth of small perturbations, discussed below. The adjoint-based sensitivity fields indicate structured patterns in the wind, thermal, and microphysical fields that project onto the model-simulated deep convection, which ultimately influences the intensification rate. For

example, sensitivity fields for Typhoon Sinlaku valid at 1200 UTC 10 September 2008 are shown in Fig. 10. At this time, Sinlaku is near its peak intensity of 125 kt, as given by the JTWC best-track estimate. The sensitivity of the final-time kinetic energy in the box shown in the figure to the initial vorticity at 800 hPa indicates a highly structured pattern with anticyclonically curved sensitivity maxima (Fig. 10a). These bands are collocated with the tropical cyclone circulation, as is apparent from the 800-hPa geopotential height and wind fields from the nonlinear forward model valid at 1200 UTC 10 September (shown in Fig. 10a), and tilt anticyclonically against the horizontal vortex shear. These anticyclonically curved maxima share characteristics with the optimal perturbations found by Nolan and Farrell (1999) in their simple-model study of vortex instability. Nolan and Farrell illustrate how finite-time optimal perturbations exhibit an initial tilt against the vortex shear, similar to that found in this case and others. Similar banded structures are apparent in the vorticity sensitivity fields for T-PARC/TCS-08 tropical cyclones that had strong circulations and, hence, significant horizontal shear around the cyclone periphery. Figure 10b shows the vertically integrated total energy (Errico 2000) of the adjoint perturbation. This quantity is a maximum near the cyclone, and is well sampled by the C130 aircraft soundings deployed during this flight. Although these vertically integrated perturbation energy plots average out the finescale features, they provided information on where the sensitivity

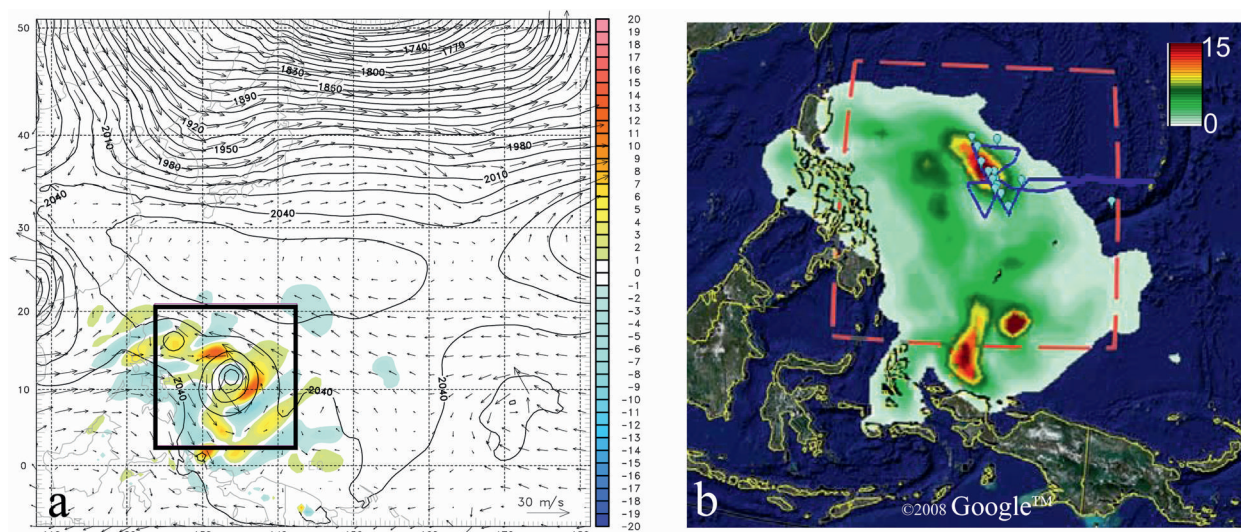


FIG. 11. The COAMPS (a) adjoint sensitivity fields for the 800-hPa vorticity ( $10^{-5} \text{ m}^2 \text{ s}^{-1}$ ) (color shading) and forward model 800-hPa geopotential heights (isopleths every 10 m) and wind vectors, and (b) vertically integrated total energy ( $\text{J kg}^{-1}$ ) based on the adjoint optimal perturbations valid at 0000 UTC 25 Sep 2008 for Typhoon Jangmi using a 36-h lead time. The C130 flight track is shown by the blue line and the dropsonde deployment locations are represented by the turquoise balloon symbols in (b). The boxes in (a) (black) and (b) (red dashed) indicate the regions over which the response function is applied. [Image for (b) was created using Google Earth.]

integrated over the depth of the atmosphere was greatest. Adjoint sensitivity images were routinely transformed into the Google Earth display software to enable the flight tracks and dropsondes to be displayed in real time along with the COAMPS forward and adjoint model results at the T-PARC/TCS-08 forecast center.

A second example of adjoint sensitivity fields, this time for the disturbance that would become Supertyphoon Jangmi, valid at 0000 UTC 25 September 2008, is shown in Fig. 11. In contrast to the previous example, which was for a mature storm, this forecast includes the formation stage of Jangmi. The COAMPS forecast started from an analysis valid for 1200 UTC 23 September 2008, before Jangmi reached tropical storm status. The JTWC upgraded the likelihood of development from “poor” to “fair” on 1300 UTC 23 September 2008, and issued its first warning at 1800 UTC 23 September 2008. JTWC estimated sustained winds of 35 kt at 0000 UTC 24 September, 50 kt at 1800 UTC 24 September, and 80 kt at 1800 UTC 25 September 2008. Thus, the forecast started before Jangmi became a tropical storm, and the adjoint calculation covers the time when Jangmi intensified from a tropical storm into a typhoon. At this time, the vorticity sensitivity at 800 hPa (Fig. 11a) gives the appearance of a wave packet characterized by a series of positive and negative sensitivity regions. The strongest regions of sensitivity correspond to regions of active convection in the model and are distributed along the axis of a monsoon trough. Given this sensitivity pattern, an observational strategy to sample in and

nearby regions of organized convection is consistent with the model sensitivity fields. The nonlinear evolution of the adjoint-derived optimal perturbations (not shown) are very similar in magnitude and structure to the tangent linear evolved perturbations in the region of the vorticity features, which lends support for the relevance of these sensitivity structures for predictability and perturbation growth in this case. The perturbation total energy (Fig. 11b) indicates three prominent maxima, one located near the region of the Jangmi circulation and two maxima positioned much farther to the south near a region of convection in the model. At this time, Jangmi had not reached hurricane strength (the estimated maximum surface wind speed at 0000 UTC 25 September was  $28 \text{ m s}^{-1}$  with a central pressure of 985 hPa). Because of the relatively large spatial region of the sensitivity, the aircraft flight on this particular day was only able to sample a part of the northern portion of the sensitivity near the Jangmi circulation. The differences in the adjoint sensitivity shown in Fig. 11a and total energy in Fig. 11b are a reflection of the dominance of the moisture and temperature sensitivities relative to the momentum sensitivity.

The corresponding sea and land surface adjoint sensitivity field is shown in Fig. 12, valid at 0000 UTC 25 September 2008. Sea and land surface temperature sensitivity products were produced routinely in real time. These products allow for a quantitative assessment of how changes to the sea surface temperature (SST) would impact storm development in the forecast and



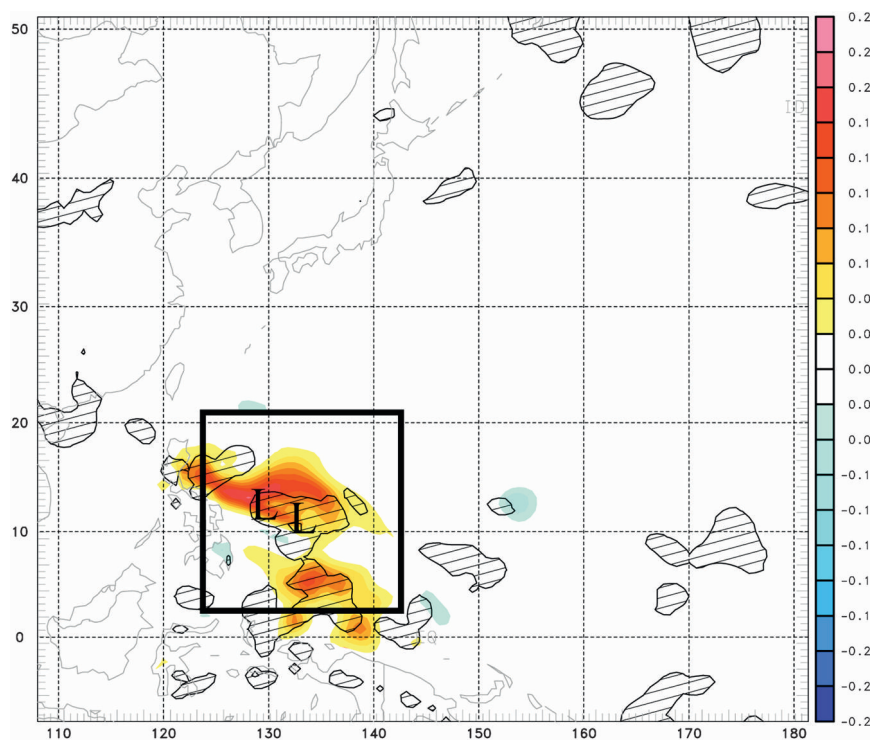


FIG. 12. The COAMPS adjoint sea and land surface sensitivity field ( $\text{K}^{-1} \text{m}^2 \text{s}^{-2}$ ) valid at 0000 UTC 25 Sep 2008 for Typhoon Jangmi using a 36-h lead time. The hatched regions denote heavy precipitation regions in excess of 20 mm during the 60-h forecast. The two low pressure symbols denote the forecast positions of the tropical cyclone center at the 36- (eastern most) and 60-h (western most) forecast times. The black box indicates the region over which the response function is applied.

provide information into where the storm forecast may be most sensitive to air–sea exchange processes. In this particular example, a relatively large region of sensitivity to the underlying sea surface is located near and to the south of the Jangmi track. The SST sensitivity is a maximum in regions where deep convection is especially vigorous in the model, as suggested by the relationship between the sensitive regions and heavy precipitation areas shown in Fig. 12. Additionally, the SST sensitivity is a maximum to the west and ahead of the TC track along the trough axis.

The evolved optimal adjoint perturbations were also made routinely available. Typical examples of evolved optimal perturbation patterns expressed as the vertically integrated total energy are illustrated in Fig. 13 for Jangmi valid at 0000 UTC 26 September and 0000 UTC 28 September based on 60-h forecasts. The corresponding sea level pressures for these two times are shown in Fig. 13 as well. At 0000 UTC 26 September (Fig. 13a), the model has a relatively weak circulation in contrast to the 0000 UTC 28 September time (Fig. 13b), which contains much stronger tropical cyclone. The model considerably underpredicts the actual intensity

because of the relatively coarse (40 km) horizontal resolution of the adjoint forecasts. At the time when the Jangmi circulation was relatively weak, the perturbation growth is relatively slow near the typhoon and actually is largest to the south near the equator associated with deep convection in the model near the southern boundary of the response function region that is not directly associated with the typhoon (Fig. 13a). However, after Jangmi intensifies further, the perturbation growth is considerably larger and more confined to the region of the tropical cyclone (Fig. 13b). In the example in Fig. 13b, a 20-fold growth of the perturbation energy occurs over the 24-h period. In general, the real-time forecasts indicate that relatively small adjoint-based basic state perturbations on the order of observational errors ( $1 \text{ m s}^{-1}$ ,  $1 \text{ K}$ ) lead to rapid growth rates in the near-surface horizontal velocity of more than  $10 \text{ m s}^{-1}$  and a 6-hPa deepening rate of the central pressure over 24 h. Additionally, the moisture perturbations often grow rapidly as well, which can have a strong coupling with the convection in the model. These regions of rapid growth typically appear to be located near the model deep convection associated with the tropical cyclone

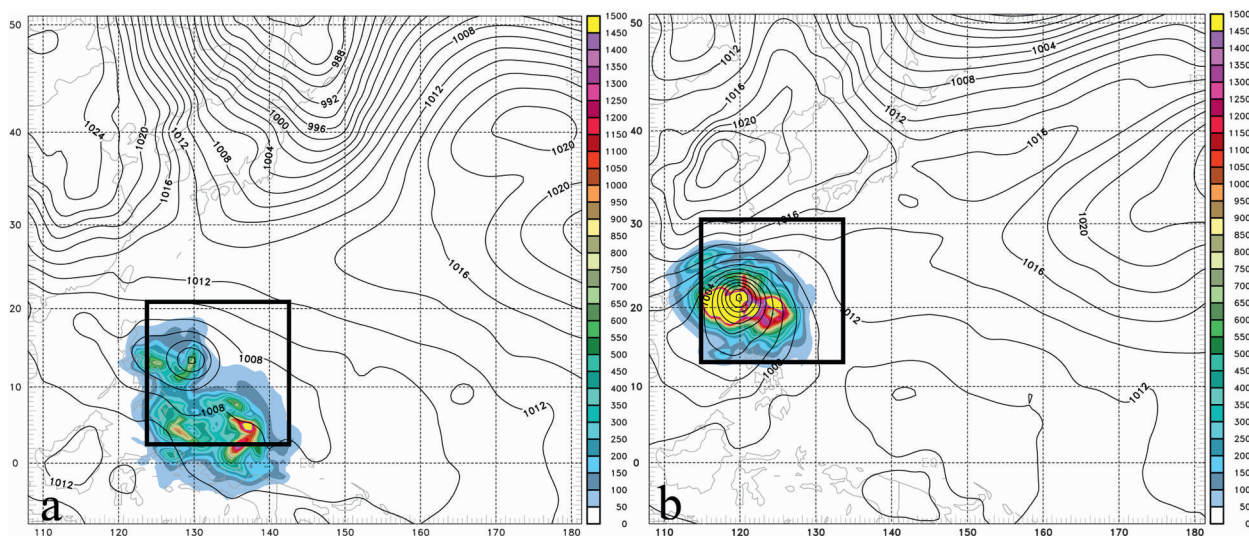


FIG. 13. The COAMPS vertically integrated total perturbation energy ( $\text{J kg}^{-1}$ ) corresponding to the evolved optimal adjoint perturbations for Typhoon Jangmi based on 60-h forecasts (36-h lead time) valid at (a) 0000 UTC 26 Sep and (b) 0000 UTC 28 Sep 2008. The sea level pressure is shown with an interval of 2 hPa. The black box indicates the region over which the response function is applied.

circulations, particularly when the circulation is weak and in the early stages of development.

#### 4. Summary and lessons learned

Both global-scale and mesoscale products were produced at the Naval Research Laboratory in support of the field phase of T-PARC/TCS-08 during August–October 2008. These products were used in conjunction with products from several other institutions to make decisions about the deployment of field program resources. The global products included SV-based targeting guidance from the NOGAPS forecast and adjoint system. These guidance products were produced for five fixed verification regions twice daily along with flow-dependent regions during high-interest periods. In addition to the SV targeting guidance, NOGAPS ensembles were also produced to help estimate uncertainty in particular forecast features and to look at potential downstream propagation of uncertainty associated with extratropical transitions of TCs. Mesoscale products included forecasts from the newly developed COAMPS-TC system. Adjoint-based mesoscale targets were produced using the COAMPS adjoint system, which includes the exact adjoint to the explicit microphysics. This is the first time a mesoscale adjoint system has been used for targeting guidance for TCs during the formation and early development stages.

Some lessons learned include the following:

- Fixed verification regions can be useful for targeted observing guidance as long as the final-time SVs are

available for inspection. This is necessary to make sure that the SVs used for targeting guidance are associated with the feature of interest, and not some other feature within the verification region.

- The NOGAPS and COAMPS targeting guidance were complementary to each other. NOGAPS products were used for assessing large-scale and remote impacts on the TC evolution over longer optimization times, and COAMPS products were used for assessing storm-scale impacts on TC evolution on finer scales and over shorter time periods, as well as influences from the near-storm environment (usually within 1500 km of the storm center).
- Results from the real-time mesoscale adjoint calculations highlight the difficulty of predicting TC formation and evolution. For example, relatively small adjoint-based perturbations on the order of observational errors ( $1 \text{ m s}^{-1}$ ,  $1 \text{ K}$ ) result in rapid growth in the near-surface horizontal velocity of more than  $10 \text{ m s}^{-1}$  and more than a 5-hPa deepening rate of the central pressure over the 24-h tangent linear forecasts. These results point to the necessity of utilizing ensembles to capture these large uncertainties associated with TCs for both developing and mature systems.

These targeted observing products were used, along with products from other centers, to make decisions about the regions where additional observations would be most helpful in improving the forecasts. Ongoing and future work with data denial experiments will help determine how effective the targeted observations were at reducing forecast errors, and will be reported on in

future papers. Because of the different optimization times and verification regions for the NOGAPS and COAMPS real-time products, direct comparisons of the sensitive regions were not feasible. Future experiments are planned to examine and compare the NOGAPS and COAMPS sensitive regions using the same optimization times and verification regions. This will allow for a comparison of these methods and for an investigation of the impacts of different resolutions and consideration of different physical processes on these adaptive observing products.

**Acknowledgments.** We gratefully acknowledge Clark Amerault for helpful discussions and the development of the adjoint and tangent linear models for COAMPS and Charles Sampson for calculating the track errors shown in Fig. 9. We also acknowledge the COAMPS-TC team of NRL, Clark Amerault, Sue Chen, Eric Hendricks, Teddy Holt, Yi Jin, Chi-Sann Liou, Keith Sasheygi, Jerome Schmidt, Shouping Wang, and Peter Black, for the development of the tropical cyclone capability within COAMPS. Support from the sponsor, ONR PE-0601153N, is gratefully acknowledged. The Department of Defense High-Performance Computing Challenge program, which provided access to real-time computational resources, is acknowledged. We thank three anonymous reviewers for comments that improved the paper.

## REFERENCES

- Aberson, S. D., 2003: Targeted observations to improve operational tropical cyclone track forecast guidance. *Mon. Wea. Rev.*, **131**, 1613–1628.
- Amerault, C., X. Zou, and J. Doyle, 2008: Tests of an adjoint mesoscale model with explicit moist physics on the cloud scale. *Mon. Wea. Rev.*, **136**, 2120–2132.
- Anwender, D., P. A. Harr, and S. C. Jones, 2008: Predictability associated with the downstream impacts of the extratropical transition of tropical cyclones: Case studies. *Mon. Wea. Rev.*, **136**, 3226–3247.
- Barkmeijer, J., R. Buizza, and T. N. Palmer, 1999: 3D-Var Hessian singular vectors and their potential use in the ECMWF Ensemble Prediction System. *Quart. J. Roy. Meteor. Soc.*, **125**, 2333–2351.
- , —, —, K. Puri, and J.-F. Mahfouf, 2001: Tropical singular vectors computed with linearized diabatic physics. *Quart. J. Roy. Meteor. Soc.*, **127**, 685–708.
- Buizza, R., 1994: Localization of optimal perturbations using a projection operator. *Quart. J. Roy. Meteor. Soc.*, **120**, 1647–1681.
- , and A. Montani, 1999: Targeting observation using SVs. *J. Atmos. Sci.*, **56**, 2965–2985.
- Cardinali, C., R. Buizza, G. Kelly, M. Shapiro, and J.-N. Thepaut, 2007: The value of observations. III: Influence of weather regimes on targeting. *Quart. J. Roy. Meteor. Soc.*, **133**, 1833–1842.
- Carr, L. E., and R. L. Elsberry, 1995: Monsoonal interactions leading to sudden tropical cyclone track changes. *Mon. Wea. Rev.*, **123**, 265–289.
- Chen, J.-H., M. S. Peng, C. A. Reynolds, and C.-C. Wu, 2009: Interpretation of tropical cyclone forecast sensitivity from the singular vector perspective. *J. Atmos. Sci.*, **66**, 3383–3400.
- Cole, H. L., and T. F. Hock, 2005: The Driftsonde Observing System development. Preprints, *13th Symp. on Meteorological Observations and Instrumentation*, Savannah, GA, Amer. Meteor. Soc., 3.4. [Available online at <http://ams.confex.com/ams/pdfpapers/94102.pdf>.]
- Daley, R., and E. Barker, 2001: NAVDAS: Formulation and diagnostics. *Mon. Wea. Rev.*, **129**, 869–883.
- Deardorff, J. W., 1980: Stratocumulus-capped mixed layers derived from a three-dimensional model. *Bound.-Layer Meteor.*, **18**, 495–527.
- Ehrendorfer, M., and J. J. Tribbia, 1997: Optimal prediction of forecast error covariances through singular vectors. *J. Atmos. Sci.*, **54**, 286–313.
- Elsberry, R. L., and P. A. Harr, 2008: Tropical cyclone structure (TCS-08) field experiment science basis, observational platforms, and strategy. *Asia-Pacific J. Atmos. Sci.*, **44**, 209–231.
- Errico, E., and K. D. Raeder, 1999: Singular-vector perturbation growth in a primitive equation model with moist physics. *J. Atmos. Sci.*, **56**, 1627–1648.
- Errico, R. M., 2000: Interpretations of the total energy and rotational energy norms applied to determination of singular vectors. *Quart. J. Roy. Meteor. Soc.*, **126**, 1581–1599.
- Gelaro, R., R. Buizza, T. N. Palmer, and E. Klinker, 1998: Sensitivity analysis of forecast errors and the construction of optimal perturbations using singular vectors. *J. Atmos. Sci.*, **55**, 1012–1037.
- , R. H. Langland, G. D. Rohaly, and T. E. Rosmond, 1999: An assessment of the SV approach to targeted observations using the FASTEX data set. *Quart. J. Roy. Meteor. Soc.*, **125**, 3299–3328.
- , T. Rosmond, and R. Daley, 2002: Singular vector calculations with an analysis error variance metric. *Quart. J. Roy. Meteor. Soc.*, **128**, 205–228.
- Giering, R., and T. Kaminski, 1998: Recipes for adjoint code construction. *ACM Trans. Math. Softw.*, **24**, 437–474.
- Harr, P. A., R. L. Elsberry, and T. F. Hogan, 2000: Extratropical transition of tropical cyclones over the western North Pacific. Part II: The impact of midlatitude circulation characteristics. *Mon. Wea. Rev.*, **128**, 2635–2653.
- , D. Jones, and S. C. Jones, 2008: Predictability associated with the downstream impacts of the extratropical transition of tropical cyclones: Methodology and a case study of Typhoon Nabi (2005). *Mon. Wea. Rev.*, **136**, 3205–3225.
- Harshvardhan, R. Davies, D. Randall, and T. Corsetti, 1987: A fast radiation parameterization for atmospheric circulation models. *J. Geophys. Res.*, **92**, 1009–1015.
- Hock, T. F., and J. L. Franklin, 1999: The NCAR GPS dropwindsonde. *Bull. Amer. Meteor. Soc.*, **80**, 407–420.
- Hodur, R. M., 1997: The Naval Research Laboratory's Coupled Ocean/Atmosphere Mesoscale Prediction System (COAMPS). *Mon. Wea. Rev.*, **125**, 1414–1430.
- , and J. D. Doyle, 1998: The Coupled Ocean/Atmosphere Mesoscale Model Prediction System (COAMPS). *Coastal Ocean Prediction*. C. N. K. Mooers, Ed., Coastal and Estuarine Studies, Vol. 56, Amer. Geophys. Union, 125–155.
- Hogan, T. F., and T. E. Rosmond, 1991: The description of the Navy Operational Global Atmospheric Prediction System's Spectral Forecast Model. *Mon. Wea. Rev.*, **119**, 1786–1815.
- Jones, S. C., and Coauthors, 2003: The extratropical transition of tropical cyclones: Forecast challenges, current understanding, and future directions. *Wea. Forecasting*, **18**, 16–56.



- Kain, J. S., 1993: Convective parameterization for mesoscale models: The Kain–Fritsch scheme. *The Representation of Cumulus Convection in Numerical Models*, Meteor. Monogr., No. 46, Amer. Meteor. Soc., 165–170.
- , and J. M. Fritsch, 1990: A one-dimensional entraining/detraining plume model and its application in convective parameterization. *J. Atmos. Sci.*, **47**, 2784–2802.
- Klemp, J., and R. Wilhelmson, 1978: The simulation of three-dimensional convective storm dynamics. *J. Atmos. Sci.*, **35**, 1070–1096.
- Langland, R. H., 2005: Issues in targeted observing. *Quart. J. Roy. Meteor. Soc.*, **131**, 3409–3425.
- , and N. L. Baker, 2004: Estimation of observation impact using the NRL atmospheric variational data assimilation system. *Tellus*, **56A**, 189–201.
- , R. Gelaro, G. D. Rohaly, and M. A. Shapiro, 1999: Targeted observations in FASTEX: Adjoint-based targeting procedures and data impact experiments in IOPs-17 and 18. *Quart. J. Roy. Meteor. Soc.*, **125**, 3241–3270.
- Leutbecher, M., J. Barkmeijer, T. N. Palmer, and A. J. Thorpe, 2002: Potential impact to forecasts of two severe storms using targeted observations. *Quart. J. Roy. Meteor. Soc.*, **128**, 1641–1670.
- Mahfouf, J., 1999: Influence of physical processes of the tangent-linear approximation. *Tellus*, **51A**, 147–166.
- Majumdar, S. J., C. H. Bishop, R. Buizza, and R. Gelaro, 2002: A comparison of ensemble transform Kalman filter targeting guidance with ECMWF and NRL total energy singular vector guidance. *Quart. J. Roy. Meteor. Soc.*, **128**, 2527–2549.
- , S. D. Aberson, C. H. Bishop, R. Buizza, M. S. Peng, and C. A. Reynolds, 2006: A comparison of adaptive observing guidance for Atlantic tropical cyclones. *Mon. Wea. Rev.*, **134**, 2354–2372.
- McLay, J., C. H. Bishop, and C. A. Reynolds, 2008: Evaluation of the ensemble transform analysis perturbation scheme at NRL. *Mon. Wea. Rev.*, **136**, 1093–1108.
- Mellor, G. L., and T. Yamada, 1974: A hierarchy of turbulence closure models for planetary boundary layers. *J. Atmos. Sci.*, **31**, 1791–1806.
- Molteni, F., R. Buizza, T. N. Palmer, and T. Petroliaigis, 1996: The ECMWF Ensemble Prediction System: Meteorology and validation. *Quart. J. Roy. Meteor. Soc.*, **122**, 73–120.
- Montani, A., and A. J. Thorpe, 2002: Mechanisms leading to singular-vector growth for FASTEX cyclones. *Quart. J. Roy. Meteor. Soc.*, **128**, 131–148.
- , —, R. Buizza, and P. Uden, 1999: Forecast skill of the ECMWF model using targeted observations during FASTEX. *Quart. J. Roy. Meteor. Soc.*, **125**, 3219–3240.
- Nolan, D. S., and B. F. Farrell, 1999: Generalized stability analyses of asymmetric disturbances in one- and two-celled vortices maintained by radial inflow. *J. Atmos. Sci.*, **56**, 1287–1307.
- Oortwijn, J., and J. Barkmeijer, 1995: Perturbations that optimally trigger weather regimes. *J. Atmos. Sci.*, **52**, 3932–3944.
- Palmer, T. N., R. Gelaro, J. Barkmeijer, and R. Buizza, 1998: Singular vectors, metrics, and adaptive observations. *J. Atmos. Sci.*, **55**, 633–653.
- Peng, M. S., and C. A. Reynolds, 2005: Double trouble for typhoon forecasters. *Geophys. Res. Lett.*, **32**, L02810, doi:10.1029/2004GL021680.
- , and —, 2006: Sensitivity of tropical cyclone forecasts as revealed by singular vectors. *J. Atmos. Sci.*, **63**, 2308–2328.
- , J. A. Ridout, and T. F. Hogan, 2004: Recent modifications of the Emanuel convective scheme in the Naval Operational Global Atmospheric Prediction System. *Mon. Wea. Rev.*, **132**, 1254–1268.
- , R. N. Maue, C. A. Reynolds, and R. L. Langland, 2007: Hurricanes Ivan, Jeanne, Karl (2004) and mid-latitude trough interactions. *Meteor. Atmos. Phys.*, **97**, 221–237.
- Puri, K., J. Barkmeijer, and T. N. Palmer, 2001: Ensemble prediction of tropical cyclones using targeted diabatic singular vectors. *Quart. J. Roy. Meteor. Soc.*, **127**, 685–708.
- Rabier, F., E. Klinker, P. Courtier, and A. Hollingsworth, 1996: Sensitivity of forecast errors to initial conditions. *Quart. J. Roy. Meteor. Soc.*, **122**, 121–150.
- Reynolds, C. A., R. Gelaro, and J. D. Doyle, 2001: Relationship between singular vectors and transient features in the background flow. *Quart. J. Roy. Meteor. Soc.*, **127**, 1731–1760.
- , T. E. Rosmond, and R. Gelaro, 2005: A comparison of variance and total energy singular vectors. *Quart. J. Roy. Meteor. Soc.*, **131**, 1975–1994.
- , M. S. Peng, S. J. Majumdar, S. D. Aberson, C. H. Bishop, and R. Buizza, 2007: Interpretation of adaptive observing guidance for Atlantic tropical cyclones. *Mon. Wea. Rev.*, **135**, 4006–4029.
- , —, and J.-H. Chen, 2009: Recurring tropical cyclones: Singular vector sensitivity and downstream impacts. *Mon. Wea. Rev.*, **137**, 1320–1337.
- Rosmond, T. E., 1997: A technical description of the NRL adjoint modeling system. NRL/MR/7532/97/7230, 53 pp.
- Rutledge, S. A., and P. V. Hobbs, 1983: The mesoscale and microscale structure of organization of clouds and precipitation in midlatitude cyclones. VIII: A model for the “seeder-feeder” process in warm-frontal rainbands. *J. Atmos. Sci.*, **40**, 1185–1206.
- Vukicevic, T., and R. M. Errico, 1993: Linearization and adjoint of parameterized moist diabatic process. *Tellus*, **45A**, 493–510.
- Wu, C.-C., and Coauthors, 2005: Dropwindsonde Observations for Typhoon Surveillance near the Taiwan Region (DOTSTAR)—An overview. *Bull. Amer. Meteor. Soc.*, **86**, 787–790.
- , J.-H. Chen, P.-H. Lin, and K.-H. Chou, 2007a: Targeted observations of tropical cyclone movement based on the adjoint-derived sensitivity steering vector. *J. Atmos. Sci.*, **64**, 2611–2626.
- , K.-H. Chou, P.-H. Lin, S. D. Aberson, M. S. Peng, and T. Nakazawa, 2007b: The impact of dropwindsonde data on typhoon track forecasts in DOTSTAR. *Wea. Forecasting*, **22**, 1157–1176.
- , and Coauthors, 2009: Intercomparison of targeted observation guidance for tropical cyclones in the northwestern Pacific. *Mon. Wea. Rev.*, **137**, 2471–2492.
- Zou, X., I. M. Navon, and J. Sela, 1993: Control of gravitational oscillations in variational data assimilation. *Mon. Wea. Rev.*, **121**, 272–289.